INTERNATIONAL JOURNAL FOR NUMERICAL METHODS IN FLUIDS
Int. J. Numer. Meth. Fluids 2007; **55**:867–897
Published online 24 April 2007 in Wiley InterScience (www.interscience.wiley.com). DOI: 10.1002/fld.1499

Coupled ghost fluid/two-phase level set method for curvilinear body-fitted grids

Juntao Huang, Pablo M. Carrica and Frederick Stern*, †

IIHR Hydroscience & Engineering, The University of Iowa, Iowa City, IA 52242, U.S.A.

SUMMARY

A coupled ghost fluid/two-phase level set method to simulate air/water turbulent flow for complex geometries using curvilinear body-fitted grids is presented. The proposed method is intended to treat ship hydrodynamics problems. The original level set method for moving interface flows was based on Heaviside functions to smooth all fluid properties across the interface. We call this the Heaviside function method (HFM). The HFM requires fine grids across the interface. The ghost fluid method (GFM) has been designed to explicitly enforce the interfacial jump conditions, but the implementation of the jump conditions in curvilinear grids is intricate. To overcome these difficulties a coupled GFM/HFM method was developed in which approximate jump conditions are derived for piezometric pressure and velocity and pressure gradients based on exact continuous velocity and stress and jump in momentum conditions with the jump in density maintained but continuity of the molecular and turbulent viscosities imposed. The implementation of the ghost points is such that no duplication of memory storage is necessary. The level set method is adopted to locate the air/water interface, and a fast marching method was implemented in curvilinear grids to reinitialize the level set function. Validations are performed for three tests: super- and sub-critical flow without wave breaking and an impulsive plunging wave breaking over 2D submerged bumps, and the flow around surface combatant model DTMB 5512. Comparisons are made against experimental data, HFM and single-phase level set computations. The proposed method performed very well and shows great potential to treat complicated turbulent flows related to ship flows. Copyright © 2007 John Wiley & Sons, Ltd.

Received 15 July 2006; Revised 1 March 2007; Accepted 3 March 2007

KEY WORDS: moving interface flows; ghost fluid method; level set method; fast marching method; curvilinear grids; ship hydrodynamics

*Correspondence to: Frederick Stern, IIHR Hydroscience & Engineering, The University of Iowa, Iowa City, IA 52242, U.S.A.
†E-mail: frederick-stern@uiowa.edu

Contract/grant sponsor: Office of Naval Research; contract/grant number: N00014-01-1-0073

1. INTRODUCTION

An important class of moving interface problems is encountered in the study of ship hydrodynamics, where air/water, high-Reynolds number turbulent flows around submerged bodies (bumps, foils, submarines, etc.) or surface-piercing bodies (surface ships) constitute a challenge. Water-based Reynolds numbers ranging from 10^6 to 10^8 in model scale and 10^8 to 10^{10} at prototype cause wall distances for $y^+ = 1$ to range between 10^{-5} and 10^{-8} L, with L the body length. A wide range of length scales with complicated air/water moving interface topologies caused by breaking waves, bubble entrainment, drop formation and air/water interactions further complicate the problem. Though current computer capabilities allow the simultaneous computation of scales ranging from the Kelvin wave pattern to bow and stern breaking waves and upcoming terascale computers could allow the incorporation of smaller spilling waves into the picture, and even wave-induced separation, capillary waves and other smaller-scale phenomena, resolving properly these phenomena is far from trivial. In addition, complex geometries are most often involved, and the large change in fluid properties between air and water step up the challenge, especially for the coupled computation of air and water wakes considering the motion of the interface. These factors make the computation of these problems particularly difficult.

Classical ship hydrodynamics approaches have treated separately the water and the air flows. Since in most applications the air/water interface behaves as a free surface, single-phase approaches either use surface tracking [1] or surface capturing [2] techniques to solve the water flow. These methods have both advantages and disadvantages, but both lack the ability of simultaneously solving the air and water flows, thus restricting their application to problems in which the air/water interface remains at constant pressure. On the other hand, the air flow has been treated assuming the air/water interface as rigid with slip conditions (the equivalent to rigid lid in water free surface computations), or simply a non-slip condition. Single-phase solvers are then used to compute problems such as the air flow in superstructures of frigates and aircraft carriers and its effect on landing safety [3–5], or the effect of the ship's superstructure on the accuracy of wind speed measurements [6, 7].

There has been recently an increasing interest on the coupled air/water flow around ships. Problems such as wind/wave interactions, air wakes for moving ships in calm water or in waves, hull damage with water-filling ship compartments, and the added resistance caused by the wind forces are important, as well as better resolution of bow and transom breaking waves. To tackle these problems, accurate and robust air/water solvers which can handle complex geometries are necessary.

The volume of fluid method (VOF) was probably the earliest surface capturing attempt to compute two-phase moving interface flows [8, 9]. In VOF methods the phase advection can be done by either algebraic or geometric methods, and different variations around the original idea have been studied [10–12]. Because of the good mass conservation characteristics, VOF has been used to simulate the flows around a surface-piercing blunt body [13], and to study pitch and heave on linear incident waves [14], among other ship hydrodynamics applications. Other surface capturing methods include front tracking methods [15] and phase-field methods [16]. By far, VOF continues to be the most popular moving interface capturing method in commercial CFD solvers, including Fluent [17] and Comet [18]. The main drawback of VOF is the complexity involved in computing geometrical quantities like distance and normal to the interface.

The level set method was originally introduced by Osher and Sethian [19] for the computation of fluid-interface problems, such as air/water dynamics, breaking surface waves, solidification-melt

DOI: 10.1002/fld

dynamics, and combustion and reacting flows. Over the past two decades, a class of numerical techniques known as level set methods have been built to capture moving interfaces in fluid flow problems, see the original work of Sussman *et al.* [20] and the reviews by Osher and Fedkiw [21] and Sethian and Smereka [22]. In the original level set method for two-phase flow, the interface is described as a thin transition region where the fluid parameters are evaluated using a smoothed Heaviside function. We call this the Heaviside function method (HFM). After using higher-order, hybrid and adaptive techniques, the level set method has become an extremely powerful and accurate tool. It should be pointed out here that the level set function must be kept as a signed distance function during the computation, which is achieved by performing periodically a reinitialization [20, 23]. Refinements to the method include faster reinitialization methods, most notably the fast marching method introduced by Sethian [24], methods with better mass conservation properties like the particle level set method [25] and the hybrid level set/VOF methods [26].

Level set methods have been applied to the water flow in ship hydrodynamics problems. Vogt and Larsson [27] used both single- and two-phase level set methods to study the flow around a submerged 2D hydrofoil in steady state. Di Mascio *et al.* [28] studied the 3D flow around a surface ship in steady state using a single-phase level set method. Carrica *et al.* [2, 29, 30] and Wilson *et al.* [31] extended the single-phase level set method to compute the unsteady viscous free surface flows around complex geometries with large amplitude motions using a dynamic overset approach, including ship motions. Cura Hochbaum and Vogt [32] computed 3D flows around container ships using a HFM in curvilinear grids, allowing for ship motions by using a non-inertial coordinate frame. Other 2D applications can be found in the literature. The main drawback of the HFM is the use of smoothed properties through the transition thickness, which makes the accuracy strongly dependent on the local grid spacing. Grid spacing can be relatively large for surface flows in ships, especially on the streamwise direction, causing large transition thicknesses and reducing the computational accuracy.

The ghost fluid method (GFM) was developed to capture the jump conditions across an interface with zero transition thickness while simulating the sharp moving interface. Fedkiw *et al.* [33] developed the GFM method and applied it to compressible flows. Liu *et al.* [34] developed a numerical method for the variable coefficient Poisson equation in the presence of interfaces where both the coefficients and the solution itself may be discontinuous. Kang *et al.* [35] extended the GFM [33] to multiphase incompressible laminar flows including the effects of viscosity and density jumps, surface tension and gravity. Liu *et al.* [36] introduced a technique for simulating droplet interactions with surfaces of arbitrary shape in laminar flow. Pijl *et al.* [37] presented a mass-conserving level set method to simulate the bubbly laminar flows, where they used approximate jump conditions with jumps in density and pressure gradient but assumed continuity of the molecular viscosity. All these efforts have used Cartesian grids.

Moureau *et al.* [38] performed a large-eddy simulation of premixed combustion, removing the steep gradients in the spatial derivatives by solving two continuous problems in the unburned and burned gases by satisfying jump conditions at the interface. The GFM was applied to a laminar two-phase moving interface problem with low density ratio using an unstructured grid [39], which to the knowledge of the authors is the first study with GFM on non-cartesian grids. Recently, Zhou *et al.* [40] developed a higher-order matched interface and boundary method. The authors compare that method with GFM or immersed interface method in detail as well. In addition, a simple finite difference scheme for the elliptic interface problem with a discontinuous diffusion coefficient was proposed using a body-fitted curvilinear coordinate system [41]. This is the only contribution known to the authors dealing with jump conditions in curvilinear grids, but the study

DOI: 10.1002/fld

is limited to analyse Poisson equations with fixed interfaces aligned with the grid lines. Though the GFM shows an enormous potential for ship hydrodynamics problems, standard GFM algorithms were developed for orthogonal coordinates, which limits their application to relatively simple geometries. It is still a challenge to implement the jump conditions in curvilinear grids.

In this paper we extend the GFM to curvilinear body-fitted coordinates, with special emphasis on the computation of air/water moving interface turbulent flows caused by 3D ships with complex geometries. The approach uses the piezometric pressure both in air and water to eliminate the gravity forces from the momentum equation. This results in two fluid flow problems with constant density, one in air and one in water, coupled by interfacial jump conditions for the pressure and pressure gradient. We assume that molecular viscosity in all equations and all fluid properties in the turbulence equations can be approximated by a smoothed Heaviside Function and are thus continuous across the interface. This results in a coupled GFM/HFM method in which approximate jump conditions are derived for piezometric pressure and velocity and pressure gradients based on the exact continuous velocity and stress and jump in momentum conditions with jump in density maintained but continuity of the molecular and turbulent viscosities imposed. The main advantage of this approach with respect to the HFM method is that it is significantly more robust and accurate with relatively coarse curvilinear grids, due to much better representation of the pressure gradients close to the interface. A full GFM would enforce also explicit jump conditions on the viscosity, velocity gradients and turbulence quantities, which would be desirable, but its implementation in curvilinear grids is problematic and requires further research. In our case we use a projection method in collocated grids to solve the Poisson equation. The level set method was adopted to capture the location of the interface, and a fast marching reinitialization algorithm was developed for curvilinear grids.

The coupled GFM/HFM method is validated by running three test cases and comparing against experimental data and computations with a single-phase level set code. The first test is the 2D steady-state air/water flow over a submerged bump, the second is the unsteady plunging wave breaking above a submerged bump, and the third is the air/water flow around a surface combatant model David Taylor Model Basin (DTMB) 5512 advancing at medium speed ($Fr = 0.28$) and high speed ($Fr = 0.41$). In all cases good agreement with the experimental data was obtained.

2. MATHEMATICAL MODEL

A one-fluid model with variable properties is adopted to compute the immiscible and incompressible two-phase flow. Both phases (air and water) are transported with a common velocity.

2.1. Governing equations

The Reynolds averaged Navier–Stokes (RANS) momentum and mass conservation equations for either water or air are written as

$$\rho\left(\frac{\partial u_i}{\partial t} + u_j\frac{\partial u_i}{\partial x_j}\right) = -\frac{\partial \hat{p}}{\partial x_i} + \frac{\partial}{\partial x_j}\left[Re_{\text{eff}}^{-1}\left(\frac{\partial u_i}{\partial x_j} + \frac{\partial u_j}{\partial x_i}\right)\right] + S_i \tag{1}$$

$$\frac{\partial u_j}{\partial x_j} = 0 \tag{2}$$

DOI: 10.1002/fld

where the piezometric pressure is

$$\hat{p} = p + \frac{\rho z}{Fr^2} + \frac{2}{3}\rho k$$

S_i is a body force due for instance to a propeller model (zero in this paper), $Re = \rho_l U_0 L_0/\mu_l$ and $Re_{\text{eff}}^{-1} = \mu/Re + \gamma_t$, with γ_t the non-dimensional turbulent viscosity, obtained from a turbulence model, $\mu = \mu_{\text{abs}}/\mu_l$, $\rho = \rho_{\text{abs}}/\rho_l$ and $Fr = U_0/\sqrt{gL}$. The subscript 'abs' stands for the absolute dimensional value of any property or variable, and U_0 and L are the reference velocity and length, usually the ship's speed and length between fore and aft perpendiculars. All variables and properties are non-dimensionalized with U_0, L and the liquid properties.

2.1.1. Coordinate transformation. The governing equations are transformed from the physical domain in Cartesian coordinates (x, y, z, t) into the computational domain in non-orthogonal curvilinear coordinates (ξ, η, ζ, τ) [42]. A partial transformation is used in which only the independent variables are transformed, leaving the velocity components U_k in the base coordinates.

2.1.2. Hydrodynamic equations. The transformed mass conservation equation reads

$$\frac{1}{J}\frac{\partial}{\partial \xi^j}(b_k^j U_k) = 0 \tag{3}$$

and the momentum equation

$$\rho\left[\frac{\partial U_i}{\partial \tau} + \frac{1}{J}\frac{\partial}{\partial \xi^j}(\breve{U}^j U_i)\right] = -\frac{1}{J} b_i^j \frac{\partial \hat{p}}{\partial \xi^j} + \frac{1}{J}\frac{\partial}{\partial \xi^j}\left[\frac{1}{J} Re_{\text{eff}}^{-1} b_l^j \left(b_l^k \frac{\partial U_i}{\partial \xi^k} + b_i^k \frac{\partial U_l}{\partial \xi^k}\right)\right] + S_i \tag{4}$$

where $\breve{U}^j = b_l^j U_l$ is the contravariant velocity.

2.1.3. Turbulence model. Menter's blended $k-\omega/k-\varepsilon$ model of turbulence is adopted [43]. The dimensionless equations for γ_t, k and ω can be written in curvilinear coordinates

$$\gamma_t = \rho\frac{k}{\omega} \tag{5}$$

$$\rho\left[\frac{\partial k}{\partial \tau} + \frac{1}{J}(b_l^j U_l)\frac{\partial k}{\partial \xi^j}\right] = \frac{1}{J}\frac{\partial}{\partial \xi^j}\left[\frac{1}{J}\left(\frac{\mu}{Re} + \sigma_k \gamma_t\right) b_l^j b_l^m \frac{\partial k}{\partial \xi^m}\right] + S_k \tag{6}$$

$$\rho\left[\frac{\partial \omega}{\partial \tau} + \frac{1}{J}(b_l^j U_l)\frac{\partial \omega}{\partial \xi^j}\right] = \frac{1}{J}\frac{\partial}{\partial \xi^j}\left[\frac{1}{J}\left(\frac{\mu}{Re} + \sigma_\omega \gamma_t\right) b_l^j b_l^k \frac{\partial \omega}{\partial \xi^k}\right] + S_\omega \tag{7}$$

with the corresponding sources

$$S_k = \gamma_t \frac{1}{J^2}\left(b_j^k \frac{\partial U_i}{\partial \xi^k} + b_i^k \frac{\partial U_j}{\partial \xi^k}\right)\left(b_j^n \frac{\partial U_i}{\partial \xi^n}\right) - \beta^* \rho \omega k \tag{8}$$

DOI: 10.1002/fld

$$S_\omega = \gamma_t \gamma \frac{\omega}{k} \frac{1}{J^2} \left(b_j^k \frac{\partial U_i}{\partial \xi^k} + b_i^k \frac{\partial U_j}{\partial \xi^k} \right) \left(b_j^n \frac{\partial U_i}{\partial \xi^n} \right) - \beta \rho \omega^2 + 2(1 - F_1) \sigma_{\omega 2} \frac{\rho}{\omega} \frac{1}{J^2} \left[\left(b_i^m \frac{\partial k}{\partial \xi^m} \right) \left(b_i^n \frac{\partial \omega}{\partial \xi^n} \right) \right] \tag{9}$$

where the blending function is computed from

$$\begin{aligned} F_1 &= \tan^{-1}(\alpha_1^4) \\ \alpha_1 &= \min \left(\max \left(\frac{\sqrt{k}}{0.09 \omega \delta}; \frac{1}{Re} \frac{500 \upsilon}{\delta^2 \omega} \right); \frac{4 \rho \sigma_{\omega 2} k}{\mathrm{CD}_{k\omega} \delta^2} \right) \\ \mathrm{CD}_{k\omega} &= \max \left(2 \rho \sigma_{\omega 2} \frac{1}{\omega} \frac{1}{J^2} \left(b_i^m \frac{\partial k}{\partial \xi^m} \right) \left(b_i^n \frac{\partial \omega}{\partial \xi^n} \right), 10^{-20} \right) \end{aligned} \tag{10}$$

2.2. Moving interface model

The essential idea in level set methods is to construct a signed distance function φ defined in the whole domain, such that the level set $\{\varphi = 0\}$ always corresponds to the position of the fluid interface. The sign of φ is arbitrarily set negative in air and positive in water. For immiscible two-phase flow, the φ governing equation is not affected by the interface and is then given by

$$\frac{\partial \varphi}{\partial t} + U \cdot \nabla \varphi = -\gamma \eta_w \tag{11}$$

where an artificial wave damping function appearing on the RHS is used to avoid wave reflections on the domain boundaries [27]. $\eta_w = \varphi + z$ is the wave elevation and γ is strength of the damping which is non-zero only near the non-reflective boundary.

2.3. Interface jump conditions

Jump conditions across the sharp air/water interface are required for the solution of the momentum, turbulence, and pressure Poisson equations. Modelling and numerical approaches are discussed, e.g. in [35, 44], respectively. The exact conditions are based on continuity of velocity and stress and jump in momentum across the interface, which lead to jump conditions for piezometric pressure and velocity and pressure gradients since the fluid properties (density and viscosity) jump across the interface.

2.3.1. Exact jump conditions. The jump function '$[\cdot]$' across the interface for an arbitrary variable ϕ is defined by

$$[\phi] = \phi^- - \phi^+ \tag{12}$$

DOI: 10.1002/fld

with the superscript '+' representing the local fluid and '−' is the other fluid. Continuous velocity requires that

$$[U_i] = 0 \tag{13}$$

Continuous stress requires that

$$[\tau_{i,j} n_j t_i] = We^{-2} kr n_i t_i \tag{14}$$

$$\tau_{i,j} = -p^* \delta_{i,j} + Re_{\text{eff}}^{-1} \left(\frac{\partial U_i}{\partial x_j} + \frac{\partial U_j}{\partial x_i} \right) \tag{15}$$

where $\mathbf{N} = (n_1, n_2, n_3) = -\nabla\varphi/|\nabla\varphi|$ is the unit normal vector (opposite sign if the local fluid is water), $kr = \nabla \cdot \mathbf{N}$ is the curvature, $\mathbf{T} = (t_1, t_2, t_3)$ is an arbitrary vector, $p^* = p + \frac{2}{3}\rho k$ and $We = U_0\sqrt{\rho_l L_0/\sigma}$ is the weber number. Substituting Equation (15) into Equation (14) and simplifying results in

$$[p^*] n_j t_j - \left[Re_{\text{eff}}^{-1} \left(\frac{\partial U_i}{\partial x_j} n_j t_i + \frac{\partial U_i}{\partial x_j} t_j n_i \right) \right] = We^{-2} kr n_j t_j \tag{16}$$

Defining $\mathbf{T}_1$ and $\mathbf{T}_2$ as unit tangent vectors that satisfy the following equations:

$$\|\mathbf{N}\| = \|\mathbf{T}_1\| = \|\mathbf{T}_2\| = 1 \tag{17}$$

$$\mathbf{N} \cdot \mathbf{T}_1 = 0 \tag{18}$$

$$\mathbf{T}_2 = \mathbf{N} \times \mathbf{T}_1 \tag{19}$$

and using jump conditions in velocity and velocity gradients in the tangential directions, the jump product identity and the continuity equation in Equation (16) results in the following normal and tangential exact jump conditions:

$$[p^*] - 2[Re_{\text{eff}}^{-1}] \left(\frac{\partial U_i}{\partial x_j} n_j n_i \right) = We^{-2} kr \tag{20}$$

$$\left(\left[\frac{\partial U_i}{\partial x_j} \right] \right) = -\frac{[Re_{\text{eff}}^{-1}]}{\widehat{Re_{\text{eff}}^{-1}}} \begin{pmatrix} \mathbf{N} \\ \mathbf{T}_1 \\ \mathbf{T}_2 \end{pmatrix}^{-1} \begin{pmatrix} 0 & 0 & 0 \\ \hat{\alpha} & 0 & 0 \\ \hat{\beta} & 0 & 0 \end{pmatrix} \left(\begin{pmatrix} \mathbf{N} \\ \mathbf{T}_1 \\ \mathbf{T}_2 \end{pmatrix}^{\mathrm{T}} \right)^{-1} \tag{21}$$

If the interface is located on the position between grid points (i, j, k) and $(i, j, k+1)$, then,

$$\hat{\alpha} = \frac{\alpha_k |\varphi_{k+1}| + \alpha_{k+1} |\varphi_k|}{|\varphi_k| + |\varphi_{k+1}|}, \quad \hat{\beta} = \frac{\beta_k |\varphi_{k+1}| + \beta_{k+1} |\varphi_k|}{|\varphi_k| + |\varphi_{k+1}|} \tag{22}$$

DOI: 10.1002/fld

where

$$\alpha = \frac{\partial U_i}{\partial x_j} n_j t_{1,i} + \frac{\partial U_i}{\partial x_j} t_{1,j} n_i \tag{23}$$

$$\beta = \frac{\partial U_i}{\partial x_j} n_j t_{2,i} + \frac{\partial U_i}{\partial x_j} t_{2,j} n_i \tag{24}$$

Applying jump conditions for the momentum equations requires that

$$\left[\frac{1}{\rho}\frac{\partial \hat{p}}{\partial x_i}\right] = \left[\frac{1}{\rho}\frac{\partial}{\partial x_j}(Re_{\text{eff}}^{-1})\left(\frac{\partial U_i}{\partial x_j} + \frac{\partial U_j}{\partial x_i}\right) + \frac{1}{\rho} Re_{\text{eff}}^{-1} \frac{\partial^2 U_i}{\partial x_j^2}\right] \tag{25}$$

where

$$\left[\frac{\mathrm{D}U_i}{\mathrm{D}t}\right] = 0 \tag{26}$$

has been used since the velocity is continuous.

Equations (13), (20), (21) and (25) are exact and difficult to implement without approximations.

2.3.2. Approximate jump conditions. Herein we assume that the density jump of 1:830 across an air/water interface is of primary importance, whereas molecular and turbulent viscosity are of secondary importance; therefore, we assume, Re_{eff}^{-1} is continuous across the interface while maintaining a jump in density. The HFM method is used to smooth Re_{eff}^{-1} across the interface, thus

$$[Re_{\text{eff}}^{-1}] = 0 \tag{27}$$

In the HFM, the fluid properties such as density and viscosity are changed across the interface using a smoothed Heaviside function introduced as

$$H(\varphi) = \begin{cases} 0 & (\varphi < -\varepsilon) \\ (\varphi + \varepsilon)/2\varepsilon + \sin(\pi\varphi/\varepsilon)/2\pi & (|\varphi| \leqslant \varepsilon) \\ 1 & (\varphi > \varepsilon) \end{cases} \tag{28}$$

where ε is the prescribed 'thickness' of the interface, taken in this paper to be twice the average grid spacing around the interface. Numerical experiments have shown that the results are fairly insensitive to the selection of ε as long as it covers less than five grid points, but a too small value may cause numerical instabilities. Thus, for an arbitrary property ϕ

$$\phi(\mathbf{x}) = \phi_{\text{a}} + (\phi_{\text{l}} - \phi_{\text{a}}) H[\varphi(\mathbf{x})] \tag{29}$$

where ϕ_{l} and ϕ_{a} are the constant values of ϕ in water and air, respectively.

If we neglect the surface tension and use Equation (27), Equation (20) becomes

$$[p^*] = 0 \tag{30}$$

Because piezometric pressure is $\hat{p} = p^* + \rho z/Fr^2$

$$[\hat{p}] = [\rho]\frac{z}{Fr^2} \tag{31}$$

DOI: 10.1002/fld

Substituting Equation (27) in Equation (21) we obtain

$$\left[\frac{\partial U_i}{\partial x_j}\right] = 0 \tag{32}$$

which means the velocity derivatives are continuous across the interface.

Even under the assumption of Equation (27) it is still difficult to obtain jump conditions for the derivative of Re_{eff}^{-1} and second-order derivatives of velocity in Equation (25). Following [35], we assume that the RHS of Equation (25) is zero as it is in inviscid flow, thus

$$\left[\frac{1}{\rho}\frac{\partial \hat{p}}{\partial x_i}\right] = 0 \tag{33}$$

This approximation is more valid for very large Reynolds number flows.

For an arbitrary variable ϕ and fluid property β, assume a jump condition

$$\left[\beta\frac{\partial \phi}{\partial x_j}\right] = S_j \tag{34}$$

and then in curvilinear coordinates

$$\left[\beta\frac{\partial \phi}{\partial \xi^k}\right]\frac{b_j^k}{J} = S_j \tag{35}$$

Therefore, in curvilinear coordinates Equation (32) becomes

$$\left[\frac{\partial U_i}{\partial \xi^j}\right] = 0 \tag{36}$$

and Equation (33) is

$$\left[\frac{1}{\rho}\frac{\partial \hat{p}}{\partial \xi^j}\right] = 0 \tag{37}$$

Note that (ξ, η, ζ) is any arbitrary curvilinear coordinate system, and thus Equations (36) and (37) hold for any line crossing the interface.

The turbulent kinetic energy is continuous across the interface. As discussed before, we use smooth Heaviside functions for all fluid properties in the turbulence model: the derivatives of the turbulent kinetic energy and the magnitude and derivatives of the turbulent dissipation rate are continuous across the interface.

3. NUMERICAL METHODS

The coupled GFM/HFM method was implemented into the code CFDShip-Iowa, a body-fitted coordinate parallel CFD code originally based on the single-phase level set method. For details on the methods and capabilities implemented in CFDShip-Iowa, the reader is directed to the papers by Carrica *et al.* [2, 29, 30] and Wilson *et al.* [31]. In the following sections we discuss details of the numerical methods as relevant for the coupled GFM/HFM method.

DOI: 10.1002/fld

3.1. Discretization strategy

We use second-order Euler backward difference for the time derivatives of all variables. For an arbitrary variable ϕ

$$\frac{\partial \phi}{\partial \tau} = \frac{1}{\Delta \tau}(1.5\varphi^n - 2\phi^{n-1} + 0.5\phi^{n-2}) \tag{38}$$

The convective terms are discretized with a second-order upwind method. Though a second-order upwind suffers from phase errors, it is more robust than more accurate higher-order methods, especially in the cases with very large density ratio in regions of sub-optimal grid quality. Taking an arbitrary control volume P on the computational domain, the convection terms for an arbitrary variable ϕ can be written as

$$\rho \frac{1}{J}\frac{\partial}{\partial \xi^j}(\breve{U}^j \phi) = \frac{1}{J}[(C_\mathrm{d}\phi_\mathrm{d} - C_\mathrm{u}\phi_\mathrm{u}) + (C_\mathrm{e}\phi_\mathrm{e} - C_\mathrm{w}\phi_\mathrm{w}) + (C_\mathrm{n}\phi_\mathrm{n} - C_\mathrm{s}\phi_\mathrm{s})] \tag{39}$$

Where u, d, w, e, s and n stand for the up $(i - \frac{1}{2})$, down $(i + \frac{1}{2})$, west $(j - \frac{1}{2})$, east $(j + \frac{1}{2})$, south $(k - \frac{1}{2})$ and north $(k + \frac{1}{2})$ faces of the control volume, respectively. For example, at down face we have

$$c_\mathrm{d} = \rho_P(\breve{U}^1)_\mathrm{d} \tag{40}$$

$$C_\mathrm{d}\phi_\mathrm{d} = \max(c_\mathrm{d}, 0)\phi_\mathrm{d}^+ - \max(-c_\mathrm{d}, 0)\phi_\mathrm{d}^- \tag{41}$$

$$\phi_\mathrm{d}^+ = 1.5\phi_i - 0.5\phi_{i-1} \tag{42}$$

$$\phi_\mathrm{d}^- = 1.5\phi_{i+1} - 0.5\phi_{i+2} \tag{43}$$

Note that the contravariant velocity in Equation (40) has to be evaluated at the cell face, which is done by linear interpolation of the node values. The metrics are computed directly at the half-cell location so as to avoid spurious sources in the evaluation of the divergence [2]. The described convective discretization is applied for all the convective terms, including the momentum, turbulence and level set equations.

The viscous terms in the momentum and turbulence equations are computed with a second-order central difference scheme. For an arbitrary variable ϕ, the diffusive term can be written as

$$\frac{1}{J}\frac{\partial}{\partial \xi^j}\left(\frac{a^{jk}}{Re_\mathrm{eff}}\frac{\partial \phi}{\partial \xi^k}\right) = D_\mathrm{d} - D_\mathrm{u} + D_\mathrm{e} - D_\mathrm{w} + D_\mathrm{n} - D_\mathrm{s} \tag{44}$$

where $a^{jk} = b_l^j b_l^k / J$ and the diffusive flux in the down direction is

$$D_\mathrm{d} = \frac{1}{J}\left(\frac{a^{1k}}{Re_\mathrm{eff}}\frac{\partial \phi}{\partial \xi^k}\right)_\mathrm{d} \tag{45}$$

Other directions are dealt with similarly. The discretization of Equation (44) leads to a 19-point stencil.

After discretization, the momentum equation takes the algebraic form

$$a_P U_i^n + \sum_\mathrm{nb} a_\mathrm{nb} U_{i,\mathrm{nb}}^n = s_{U_i} - \frac{1}{J} b_i^l \frac{\partial \hat{p}^n}{\partial \xi^l} \tag{46}$$

DOI: 10.1002/fld

where a_P is the pivot and a_{nb} are the neighbour coefficients, respectively, s_{U_i} is the source term including the variables from the previous time step arising from Equation (38), cross-derivative terms and source term of the momentum equation, n represents the non-linear iteration. The transport velocity is the latest available and causes the system to be non-linear.

3.2. Pressure Poisson equation

We use a projection algorithm [45] to satisfy mass conservation, Equation (2). PISO algorithms have been successfully used in CFDShip-Iowa in previous versions, but the projection method is much more compatible to the special form of jump conditions enforced here since it does not carry the pivot coefficient in Equation (46) into the pressure Poisson equation.

The momentum equation Equation (4) can be expressed as

$$\frac{\partial \mathbf{U}}{\partial \tau} + \frac{1}{\rho}\nabla \hat{p} = \mathbf{V} \tag{47}$$

where $\mathbf{V}$ is a differential expression of $\mathbf{U}$ representing the rest of the terms in the momentum equation not explicitly shown in Equation (47). Taking the divergence of Equation (47) and noting that $\nabla \cdot (\partial \mathbf{U}/\partial \tau) = 0$, then

$$\nabla \cdot \frac{1}{\rho}\nabla \hat{p} = \nabla \cdot \mathbf{V} \tag{48}$$

Equation (48) is a Poisson equation for the pressure. The resulting pressure is used to explicitly update the velocity field by solving

$$\frac{\partial \mathbf{U}}{\partial \tau} = \mathbf{P}(\mathbf{V}) = \mathbf{V} - \frac{1}{\rho}\nabla \hat{p} \tag{49}$$

where $\mathbf{P}(\mathbf{V})$ is the projection vector. Details of the discrete form of Equations (47)–(49) are important and are discussed next. At the current time n, we compute $\mathbf{V}$ from the left-hand side of Equation (47) using an estimated value $\mathbf{U}^{*,k}$, which is the latest available velocity vector

$$\mathbf{V} = \frac{1}{\Delta \tau}(1.5\mathbf{U}^{*,k} - 2\mathbf{U}^{n-1} + 0.5\mathbf{U}^{n-2}) + \frac{1}{\rho^{n,k}}\nabla \hat{p}^{n,k} \tag{50}$$

Let the projection vector be

$$\mathbf{P}(\mathbf{V}) = \mathbf{V}_{\text{d}} = \frac{1}{\Delta \tau}(1.5\mathbf{U}^{n,k+1} - 2\mathbf{U}^{n-1} + 0.5\mathbf{U}^{n-2}) \tag{51}$$

introducing Equation (47) we obtain

$$\mathbf{V}_{\text{d}} + \frac{1}{\rho^{n,k+1}}\nabla \hat{p}^{n,k+1} = \mathbf{V} \tag{52}$$

and Equation (48) has the form

$$\nabla \cdot \left(\frac{1}{\rho^{n,k+1}}\nabla \hat{p}^{n,k+1} \right) = \nabla \cdot \mathbf{V} \tag{53}$$

DOI: 10.1002/fld

After solving Equation (53) for the pressure, the projection vector is obtained

$$\mathbf{V}_{\mathrm{d}} = \mathbf{V} - \frac{1}{\rho^{n,k+1}} \nabla \hat{p}^{n,k+1} \tag{54}$$

and the updated velocity can then be written as

$$\mathbf{U}^{n,k+1} = \mathbf{U}^{*,k} + \frac{\Delta\tau}{1.5} (\nabla \hat{p}^{n,k}/\rho^{n,k} - \nabla \hat{p}^{n,k+1}/\rho^{n,k+1}) \tag{55}$$

In our implicit scheme, Picard iterations are used to converge the non-linear convective term in the momentum equations. The updated velocity obtained from Equation (55) is substituted into Equation (46), and a new velocity is obtained. This way the pressure and velocity are iterated to convergence. The Poisson Equation (53) in curvilinear grids is written as

$$\frac{\partial}{\partial \xi^j} \left(E^{jl} \frac{\partial \hat{p}}{\partial \xi^l} \right) = \hat{d} \tag{56}$$

where $p^{n,k+1}$ was replaced by p, and

$$E^{jl} = \frac{b_i^j b_i^l}{J \rho^{n,k+1}} \tag{57}$$

$$\hat{d} = \breve{V}_{\mathrm{d}}^1 - \breve{V}_{\mathrm{u}}^1 + \breve{V}_{\mathrm{e}}^2 - \breve{V}_{\mathrm{w}}^2 + \breve{V}_{\mathrm{n}}^3 - \breve{V}_{\mathrm{s}}^3 \tag{58}$$

The contravariant velocities at the cell faces are computed by averaging. For instance, in the down face

$$\breve{V}_{\mathrm{d}}^1 = (b_l^1)_{i+1/2} \frac{V_{l,i} + V_{l,i+1}}{2} \tag{59}$$

The contravariant pressure gradient is expressed as

$$\breve{\nabla} \hat{p}^j = E^{jl} \frac{\partial \hat{p}}{\partial \xi^l} \tag{60}$$

and computing the divergence similar to Equation (58) we obtain

$$\breve{\nabla} \hat{p}_{\mathrm{d}}^1 - \breve{\nabla} \hat{p}_{\mathrm{u}}^1 + \breve{\nabla} \hat{p}_{\mathrm{e}}^2 - \breve{\nabla} \hat{p}_{\mathrm{w}}^2 + \breve{\nabla} \hat{p}_{\mathrm{n}}^3 - \breve{\nabla} \hat{p}_{\mathrm{s}}^3 = \hat{d} \tag{61}$$

To guarantee a strong pressure/velocity coupling, discretization of the contravariant pressure gradients is made on the cell faces. For example,

$$\begin{aligned} \breve{\nabla} \hat{p}_{\mathrm{d}}^1 = {} & E_{i+1/2}^{11} (\hat{p}_{i+1,j,k} - \hat{p}_{i,j,k}) + \frac{E_{i+1/2}^{12}}{4} (\hat{p}_{i,j+1,k} - \hat{p}_{i,j-1,k} + \hat{p}_{i+1,j+1,k} - \hat{p}_{i+1,j-1,k}) \\ & + \frac{E_{i+1/2}^{13}}{4} (\hat{p}_{i,j,k+1} - \hat{p}_{i,j,k-1} + \hat{p}_{i+1,j,k+1} - \hat{p}_{i+1,j,k-1}) \end{aligned} \tag{62}$$

DOI: 10.1002/fld

Curvilinear coordinates lead to a 19-point stencil for the pressure equation. The discrete form of Equation (61) is

$$a_p \hat{p}_p + \sum_{\mathrm{nb}=1}^{18} a_{\mathrm{nb}} \hat{p}_{\mathrm{nb}} = b \tag{63}$$

where a_p is the diagonal component of the pressure matrix, a_{nb} are the off-diagonal coefficients and b is the right-hand side term (RHS).

3.3. Ghost pressure at ghost points

The density is implicit in the coefficients of Equations (56)–(58), which is discontinuous across the interface, and causes the pressure and pressure gradient to be discontinuous. Fedkiw *et al.* [33] and Zhou *et al.* [40] used ghost points in the other fluid in a Cartesian grid to explicitly enforce the jump conditions. Following the ideas of Carrica *et al.* [2] for enforcing the interfacial pressure in a curvilinear grid with the single-phase level set method, we develop a general expression for the ghost pressure on any neighbour point in a different fluid for general structured curvilinear grids.

Figure 1 shows the position of grids points P and Q across the interface in an arbitrary curvilinear coordinate, where the point P is located in the local fluid '+', and Q is a neighbour of P in the other fluid.

We will first apply the jump condition in Equation (37) (recall we can write this jump condition along any line, coincident or not with a grid coordinate line). Assume that the line joining the computational point P and its neighbour Q has a coordinate χ that varies from 0 at P to 1 at Q. The jump condition Equation (37) is then

$$\left[\beta \frac{\partial \hat{p}}{\partial \chi}\right] = 0 \tag{64}$$

with $\beta = 1/\rho$. Equation (64) can be discretized as

$$\beta^- \frac{\hat{p}_Q - \hat{p}_I^-}{1-\lambda} - \beta^+ \frac{\hat{p}_I^+ - \hat{p}_P}{\lambda} = 0 \tag{65}$$

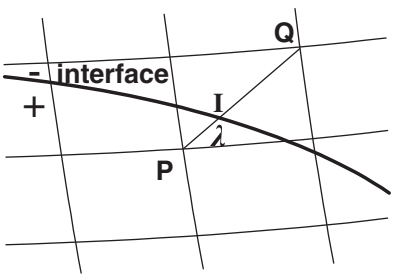

Figure 1. Interpolation scheme and ghost points.

DOI: 10.1002/fld

where $\lambda = \varphi_P/(\varphi_P - \varphi_Q)$ is the location of the interface in χ coordinates. The second jump condition from Equation (31), together with the jump condition for ρ from Equation (12) is

$$\hat{p}_I^- - \hat{p}_I^+ = (\rho^- - \rho^+)\frac{z_I}{Fr^2} \tag{66}$$

with $z_I = (1-\lambda)z_P + \lambda z_Q$. From Equations (65) and (66) we obtain the piezometric pressure at the interface for each fluid

$$\begin{aligned} \hat{p}_I^+ &= \frac{\lambda\beta^-}{\overline{\beta}}\hat{p}_Q + \frac{(1-\lambda)\beta^+}{\overline{\beta}}\hat{p}_P - \lambda\frac{\beta^-}{\overline{\beta}}\frac{z_I}{Fr^2}[\rho] \\ \hat{p}_I^- &= \frac{\lambda\beta^-}{\overline{\beta}}\hat{p}_Q + \frac{(1-\lambda)\beta^+}{\overline{\beta}}\hat{p}_P + \left(1 - \lambda\frac{\beta^-}{\overline{\beta}}\right)\frac{z_I}{Fr^2}[\rho] \end{aligned} \tag{67}$$

where $\overline{\beta} = (1-\lambda)\beta^+ + \lambda\beta^-$. The ghost pressure at point Q can then be extended from point P and I from fluid '+'

$$\hat{p}_P^{G+} = \hat{p}_I^+ + \frac{(1-\lambda)}{\lambda}(\hat{p}_I^+ - \hat{p}_Q) \tag{68}$$

then

$$\hat{p}_Q^{G+} = \frac{\beta^-}{\overline{\beta}}\hat{p}_Q + \left(1 - \frac{\beta^-}{\overline{\beta}}\right)\hat{p}_P - \frac{\beta^-}{\overline{\beta}}\frac{z_I}{Fr^2}[\rho] \tag{69}$$

If points P and Q are located in the same fluid, it is obvious that $\hat{p}_Q^{G+} = \hat{p}_Q$. Substituting Equation (69) into Equation (63) with Q any neighbour point, the new matrix coefficients as a function of the old coefficients are

$$a_p = a_p + \sum_{\mathrm{nb}=1}^{18} a_{\mathrm{nb}}\left(1 - \frac{\beta^-}{\overline{\beta}}\right)_{\mathrm{nb}} \tag{70}$$

$$b = b + \sum_{\mathrm{nb}=1}^{18} a_{\mathrm{nb}}\left(\frac{\beta^-}{\beta}\frac{z_I}{Fr^2}[\rho]\right)_{\mathrm{nb}} \tag{71}$$

$$a_{\mathrm{nb}} = a_{\mathrm{nb}}\frac{\beta^-}{\overline{\beta}} \tag{72}$$

The resulting Poisson equation has the jump conditions embedded. The pressure gradient in each fluid is then computed using the ghost pressures. The problem is then decomposed into two problems with constant density coupled by the jump conditions. When the density ratio is large, the system becomes stiff and the resulting linear system is ill-conditioned. We stress that the ghost pressure is a function of the actual pressures at two neighbour points on each side of the interface, therefore the ghost pressures are never stored in memory.

3.4. Fast marching method

As the computation evolves, the transport of the level set function φ will not keep it as a distance function (i.e. $|\nabla\varphi| \neq 1$), which causes the computation to lose precision. One of the typical

DOI: 10.1002/fld

reinitialization methods is to solve a transient differential equation [20, 21], but the method does not work well when very large aspect ratio cells are used. Carrica *et al.* [2] used a coupled close point and partial differential equation method to reinitialize the level set function in curvilinear grids. Though it works well for curvilinear grids and is robust, the method is not very fast.

We propose a reinitialization method that builds on the close point reinitialization of Carrica *et al.* [2], but uses an extension of the fast marching method of Adalsteinsson and Sethian [46]. The close point technique can both prevent the interface from moving during the stage of reinitialization and supply the initial values at the beginning of fast marching step. Grid points farther away from the interface are reinitialized using

$$\begin{cases} |\nabla\varphi| = 1 \\ \varphi|_\Gamma = 0 \end{cases} \tag{73}$$

Godunov methods are usually adopted to solve this equation [46, 47].

The central idea behind the fast marching method is to systematically advance the front in an upwind fashion to produce the solution of φ, building the solution outward from the smallest φ value in the $\varphi>0$ region, and from the greatest φ value in the $\varphi<0$ region. Detailed description of the technique can be found in [24, 46, 48], while we will focus on the implementation on curvilinear coordinates. Discussion will centre on the case of $\varphi>0$, but the method is similar for $\varphi<0$.

We follow Sethian's [24, 48] definitions for all points, thus classifying the points into far, close and accepted. We only discuss how to compute the φ values of all neighbour points (apart from accepted) of the trial point changed from close to accepted in a curvilinear grid, and we call those points to be computed as tagged points. We focus on one of these tagged points and begin to look for its neighbour points, and if there are three accepted points on different coordinate ξ, η, ζ with level set value of φ_1, φ_2, φ_3, respectively, and according to Equation (73), we can get following equation:

$$\sum_{i=1}^{3}\left(\frac{\partial\varphi}{\partial x_i}\right)^2 = \sum_{i=1}^{3}\left[\sum_{j=1}^{3}\frac{b_i^j}{J}\frac{\partial\varphi}{\partial\xi^j}\right]^2 = \sum_{i=1}^{3}\left[\sum_{j=1}^{3}\frac{b_i^j}{J}(\varphi-\varphi_j)\right]^2 = 1 \tag{74}$$

which is rewritten as the quadratic equation

$$a\varphi^2 + b\varphi + c = 0 \tag{75}$$

and

$$a = \frac{1}{J^2}\left[\sum_{k=1}^{3}\sum_{j=1}^{3}\sum_{i=1}^{3} b_k^i b_k^j\right], \quad b = -2\frac{1}{J^2}\sum_{k=1}^{3}\left(\sum_{j=1}^{3}\sum_{i=1}^{3}(b_j^k b_j^i)\right)\varphi_k$$

$$c = \frac{1}{J^2}\sum_{k=1}^{3}\sum_{j=1}^{3}\left(\sum_{i=1}^{3} b_i^j b_i^k\right)\varphi_j\varphi_k - 1 \tag{76}$$

then select the smaller positive solution of the above equation. If we cannot find any accepted points as neighbours of the tagged point along the coordinate ξ^j, we set $\partial\varphi/\partial\xi^j = 0$ in Equation (74), otherwise if there are two accepted points on the same coordinate line we select the one with

DOI: 10.1002/fld

the smallest φ value. Through the procedure introduced in [24, 48], the level set information will propagate 'one way' from the interface out.

4. COMPUTATION EXAMPLES

We present three examples, a 2D super- and sub-critical steady-state flow over a submerged bump without wave breaking, a plunging breaking wave over an impulsively accelerated submerged bump, and the 3D flow around a surface combatant model DTMB 5512 at two different speeds. Results are compared against experimental data and other numerical methods.

Since the solution method is unsteady, steady-state solutions are obtained by running long enough to reach an asymptotic solution. Computations are impulsively started from a initial guess, i.e. free-stream at all grid points except for non-slip boundaries ($\mathbf{U}=(1,0,0)$, $\hat{p}=0$, $\varphi=-z$). This impulsive start-up condition does not satisfy continuity, since the initial condition is not divergence-free, but after a few time steps a solenoidal solution develops. This procedure is thus appropriate for the example applications shown in this paper in which the first instants of the computation are unimportant.

The boundary conditions for all variables are listed in Table I. Slip conditions are imposed by setting to zero the appropriate contravariant velocity. For instance, if $j=1$ ($\eta=\text{const}$) is a slip surface,

$$\begin{aligned} U_\xi &= \frac{1}{J}[u(i,2,k)b_1^1 + v(i,2,k)b_2^1 + w(i,2,k)b_3^1] \\ U_\eta &= 0 \\ U_\zeta &= \frac{1}{J}[u(i,2,k)b_1^3 + v(i,2,k)b_2^3 + w(i,2,k)b_3^3] \end{aligned} \tag{77}$$

Other faces and directions have similar conditions.

Table I. Boundary conditions for all variables.

	φ	p	k	ω	u	v	w
Inlet	$\frac{\partial\varphi}{\partial n}=0$	$p=0$	$k_{fs}=\frac{9\times10^{-03}}{Re}\frac{\mu}{\rho}$	$\omega_{fs}=9$	$u=1$	$v=0$	$w=0$
Exit	$\frac{\partial\varphi}{\partial n}=0$	$\frac{\partial p}{\partial n}=0$	$\frac{\partial k}{\partial n}=0$	$\frac{\partial\omega}{\partial n}=0$	$\frac{\partial^2 u}{\partial n^2}=0$	$\frac{\partial^2 v}{\partial n^2}=0$	$\frac{\partial^2 w}{\partial n^2}=0$
Far field	$\frac{\partial\varphi}{\partial n}=0$	$p=0$	$\frac{\partial k}{\partial n}=0$	$\frac{\partial\omega}{\partial n}=0$	$\frac{\partial u}{\partial n}=0$	$\frac{\partial v}{\partial n}=0$	$\frac{\partial w}{\partial n}=0$
Symmetry (y = 0)	$\frac{\partial\varphi}{\partial n}=0$	$\frac{\partial p}{\partial n}=0$	$\frac{\partial k}{\partial n}=0$	$\frac{\partial\omega}{\partial n}=0$	$\frac{\partial u}{\partial n}=0$	$v=0$	$\frac{\partial w}{\partial n}=0$
Slip	$\frac{\partial\varphi}{\partial n}=0$	$\frac{\partial p}{\partial n}=0$	$\frac{\partial k}{\partial n}=0$	$\frac{\partial\omega}{\partial n}=0$	Equation (77)	Equation (77)	Equation (77)
Non-slip	$\frac{\partial\varphi}{\partial n}=0$	Equation (56)	$k=0$	$\omega=\frac{60}{Re\,\beta y^+}\frac{\mu}{\rho}$	$u=0$	$v=0$	$w=0$

DOI: 10.1002/fld

4.1. Flow over a submerged bump

The study of the air/water flow over a submerged bump is a typical problem to validate moving interface methods. We select a 2D bump with topography [49]

$$z = -H + \frac{27E}{4}x(x-1)^2 \tag{78}$$

where H is the undisturbed water depth and E is the bump height, both non-dimensionalized with the bump length. The bump is placed on the bottom of a channel and at $t=0$ a velocity $U=1$ is imposed. For the cases studied here a final steady-state solution is achieved. Three cases with different water depth were selected, as described in Table II.

The computation domain extends from $-8<x<9$, $-H<z<2$. Since CFDShip-Iowa is a 3D code, an arbitrary thickness of 0.2 was assigned in the y direction, where five grid points are necessary to simulate a 2D problem. A numerical beach was used on the regions $-8<x<-4$ and $7<x<9$ to avoid wave reflections on the inlet and exit boundaries. The air/water transition thickness was set to 0.05. Using properties at normal conditions, the air/water density ratio is 1.2×10^{-3} and the viscosity ratio is 1.8×10^{-2}.

Since we are concerned with the gravity wave and not interested in the flow near the bump, we use a slip condition at the bump surface and solve a laminar problem. In Figures 2–4 the free surface profiles obtained by computation with the single-phase method and two-phase GFM/HFM are compared against the experimental data by Cahouet [49], for the three cases listed in Table II.

Table II. Conditions for the 2D steady-state flow over submerged bump tests.

	$Fr_L = U_0/\sqrt{gL}$	$Re = \rho_l U_0 L/\mu_l$	H	E	Grid size
Case 1	1.0	8.52E+05	0.228	0.1	$245\times5\times63$
Case 2	0.426	3.63E+05	0.670	0.1	$245\times5\times131$
Case 3	0.304	3.00E+05	0.500	0.1	$245\times5\times111$

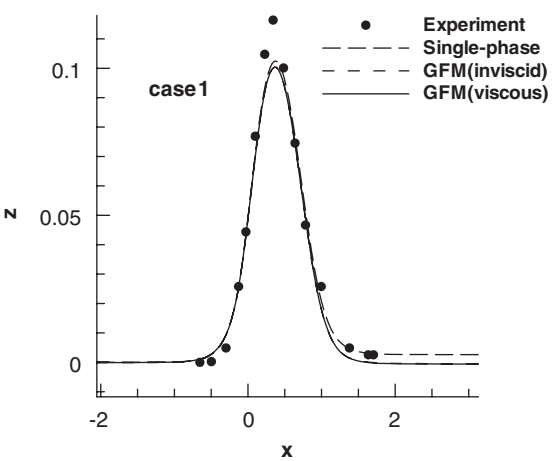

Figure 2. Interface elevation for Case 1 ($Fr_L = 1.0$).

DOI: 10.1002/fld

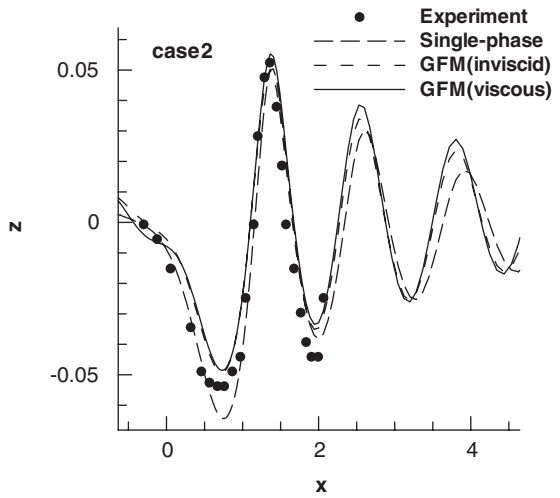

Figure 3. Interface elevation for Case 2 ($Fr_L = 0.426$).

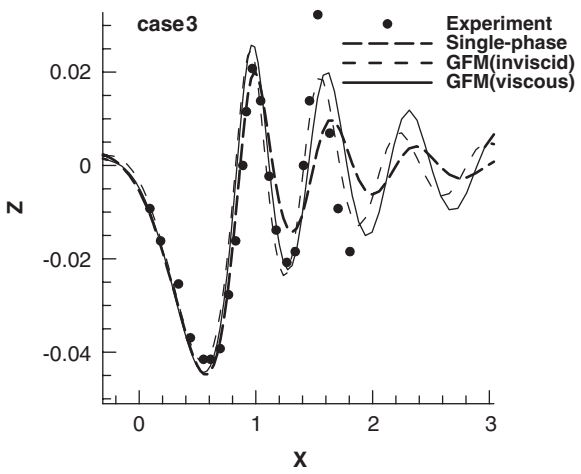

Figure 4. Interface elevation for Case 3 ($Fr_L = 0.304$).

For the supercritical flow of Case 1 the predictions by single-phase level set and GFM/HFM methods are similar, with maximum difference in the crest region; results with similar trends were shown for this geometry using HFM [50]. For the two subcritical flow Cases 2 and 3 the GFM/HFM and single-phase results are close to the experiment data both in amplitude and phase (see Figures 3 and 4), with slightly better results for GFM/HFM. Distinction is made in Figures 3 and 4 between solutions with viscous and inviscid conditions. The inviscid condition is forced by using a very large Reynolds number. In the case of inviscid flow, there is no jump in the momentum equations and thus the method becomes a GFM method. As can be seen in Figures 3 and 4, results are comparable for viscous and inviscid conditions.

DOI: 10.1002/fld

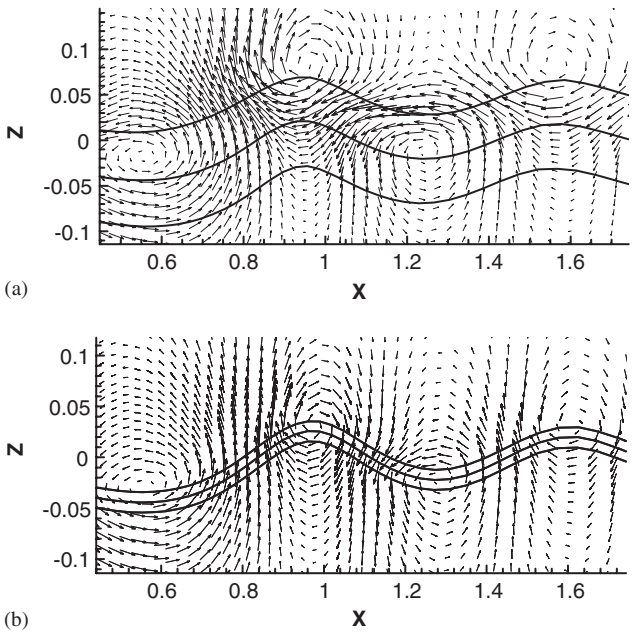

Figure 5. Velocity vectors on the earth system for Case 3: (a) HFM and (b) GFM/HFM.

Figure 5 shows the velocity field in the earth system of reference. Solutions in air and water are shown for both the standard HFM and the GFM/HFM method. The general vector fields in the water look correct for both methods, showing an orbital surface velocity as the wave passes in the direction of the bump. On the air side, however, the HFM solution exhibits vortices that are too high, almost at the location of the end of the transition region in the air. This is caused by the artificial thickness introduced to smooth the fluid properties, and cannot be set arbitrarily small but has to cover 5–10 grid points for numerical stability. GFM/HFM does not show that problem, and the transition thickness for viscosity can be much smaller to keep the computation stable, thus maintaining a sharper interface. This ability of modelling a sharp interface makes the GFM/HFM method significantly less demanding than the HFM method in terms of grid size.

4.2. Plunging wave breaking over a submerged bump

An air/water impulsive plunging breaking wave with INSEAN's smooth bump [51] is studied. The geometry of bump is given by

$$z = -h + d\left(1 - 2\frac{x^2}{a^2} + \frac{x^4}{a^4}\right), \quad x \in (-a, a) \tag{79}$$

where, h is the water depth, a is the bump half length and d is the bump height. The reference length is the bump's half length, and so $h = 0.844$, $a = 1$ and $d = 0.4$. $Fr = 0.317$ and $Re = 1.51 \times 10^5$. The 2D computational domain extents are $-8 < x < 9$, $-h < z < 2$, with 461×191 grid points. Initially, the fluid is stagnant and the flow is suddenly accelerated from that state. Non-slip boundary conditions are used on the bump surface and bottom boundary, inlet, exit and far field are set on

DOI: 10.1002/fld

other boundaries. Blended k–ε/k–ω and DES turbulence models [52] are used. A numerical beach is used in the upstream and downstream far regions to avoid wave reflections on the inlet and exit boundaries. The evolution of the interface location computed by GFM and from experiments [53] are presented in Figure 6.

The numerical results are able to capture the initial stages of plunging breaker, including the initial overturning of the wave, air entrapment, the first splash after the jet impact, and the second splash, all matching well with the experimental data. At the later stage the wave gets swept downstream and due to the presence of too many bubbles in the flow, it is difficult to visualize any distinct structures from the EFD photographs and thus comparison becomes more difficult.

Figure 7 shows the velocity distribution corresponding to the time of first splash ($t = 1.975$), displaying a complex vortex structure and an interfacial shear layer near the wave breaking region, resolving correctly the bulge, toe, impacting point, splash tongue, and bubble. Figure 8 also displays the distribution of piezometric pressure at the first splash. Note the discontinuity across the interface, and the large pressure present at the impact point, which later will cause the splash up shown in Figure 6 at $t = 2.1$.

4.3. Free surface flow around a surface combatant

The problem under study is a US Navy surface combatant restrained from motions, advancing in calm water with sinkage and trim fixed at the dynamic condition. The ship is the bare hull DTMB model 5512, a 1:46.6 model scale of a modern surface combatant. The geometry is a benchmark on the ship hydrodynamics community, tested in the towing tanks at DTMB, IIHR (Iowa) and INSEAN (Italy), and selected as test case for code validation at the Ship Hydrodynamics CFD workshops in Gothenburg 2000 [54] and Tokyo 2005 [55]. Numerical results are compared and validated in this work against the data taken at the IIHR towing tank by Gui *et al.* [56] and Longo and Stern [57].

Simulations are performed at medium and high speed, corresponding to Froude numbers $Fr = 0.28$ and 0.41, and Reynolds numbers of $Re = 4.85 \times 10^6$ and 7.10×10^6. Air/water density and viscosity ratios are 1.2×10^{-3} and 1.8×10^{-2}, respectively. Experimental data are available for resistance and wave profiles for both Froude numbers, and free surface field and nominal wake plane velocities for $Fr = 0.28$.

A double-O topology grid was generated with a hyperbolic solver. A slightly curved bare deck was added to analyse the air flow. The domain extents are $-0.7 < x < 2$, $0 < y < 1$, $-1 < z < 0.6$. The total number of grid points was 615 000, distributed in 16 blocks for parallel processing. Since the problem is symmetric, only a half ship was computed and symmetry boundary conditions used. The whole far field was set to inlet boundary condition, while non-slip was used at the ship hull. The grid spacing on the first grid point away from the wall was set such that $y^+ < 1$.

Figure 9 shows the time history of the resistance coefficient, defined as

$$C_T = \frac{F_x}{\frac{1}{2}\rho_l U_0^2 A_\mathrm{s}} \tag{80}$$

where A_s is the static wetted area of the ship. The resistance coefficient was computed integrating forces separately in water and air. After some time needed to develop the Kelvin waves and the ship's boundary layer, the force coefficients converge to a steady-state value for both the Froude numbers. The final resistance coefficient, shown in Table III, is around 6% higher than in the experiment for both Froude numbers. These differences are within typical values for RANS

DOI: 10.1002/fld

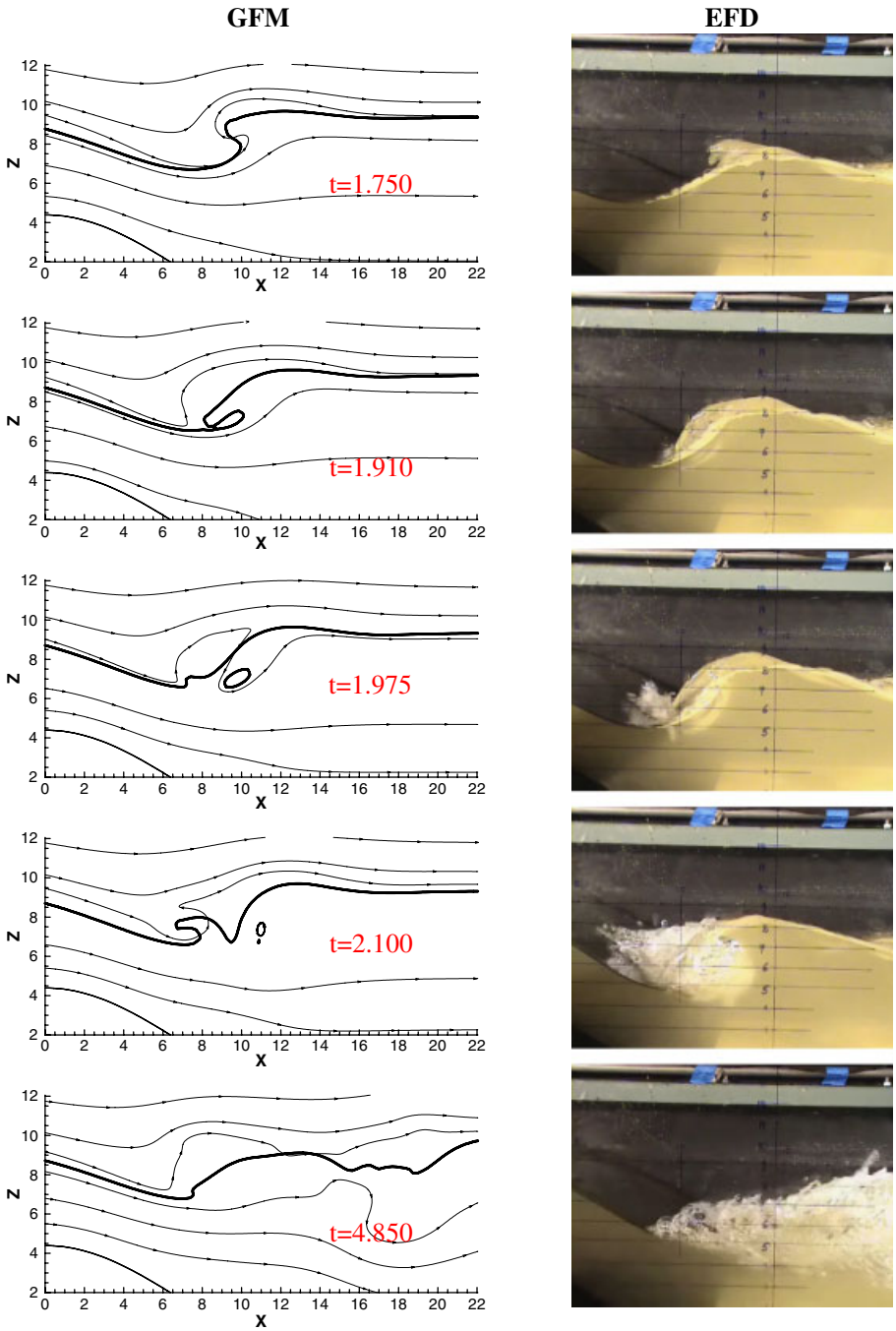

Figure 6. Comparison of CFD and EFD for an impulsive plunging wave.

DOI: 10.1002/fld

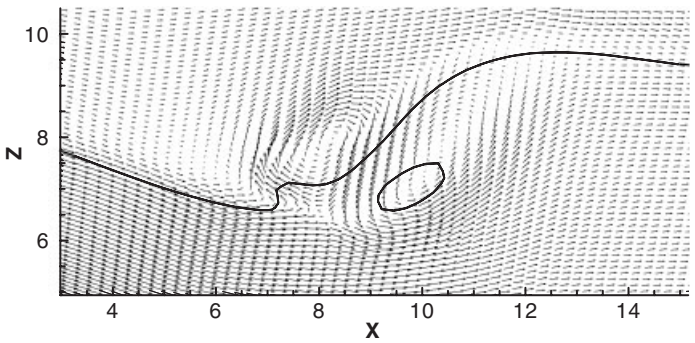

Figure 7. Velocity distribution at time = 1.975 (first splash).

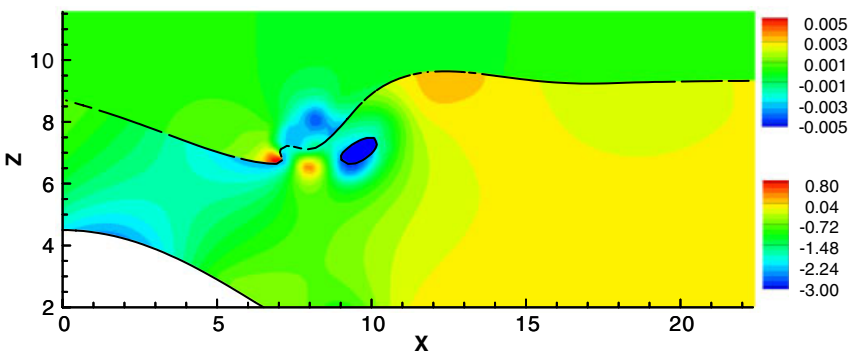

Figure 8. Pressure distribution at time = 1.975 (upper and lower legends correspond to air and water regions).

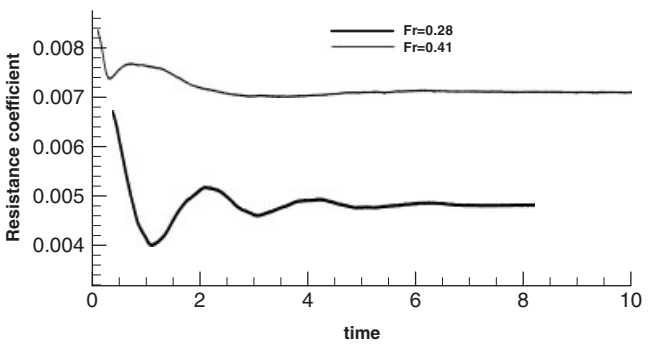

Figure 9. Convergence history of the resistance coefficient.

DOI: 10.1002/fld

Table III. CFD predictions of resistance and comparison with EFD results.

	CFD air/water	Air/water ratio (%)	Total (Experiment)	Total (CFD)	(CFD − EFD)/EFD (%)
$Fr = 0.28$	0.000061/0.00483	1.26	0.00461	0.00489	6.1
$Fr = 0.41$	0.0000073/0.00711	1.03	0.00673	0.00718	6.7

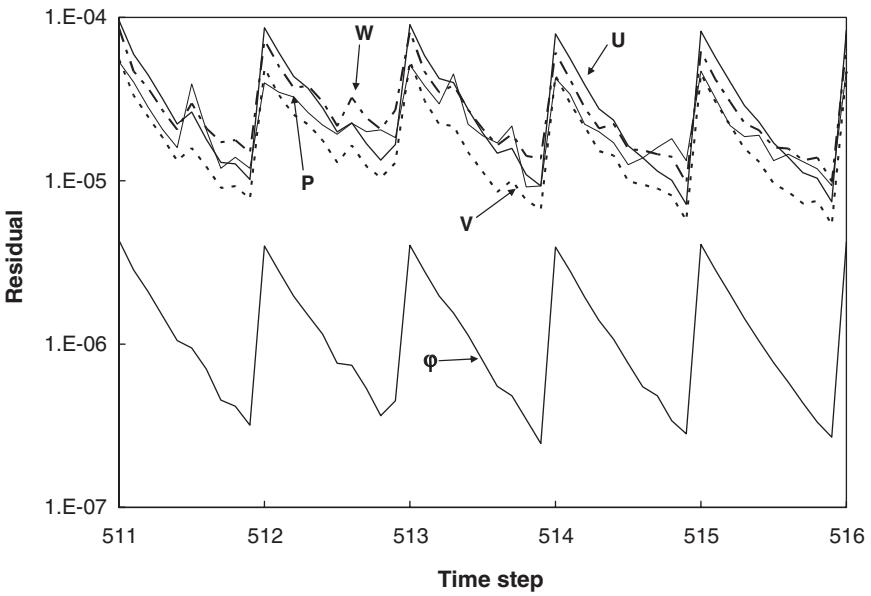

Figure 10. Typical convergence history of the non-linear iterations, $Fr = 0.28$.

resistance computations. Figure 10 shows the typical convergence history of the non-linear Picard iterations from time 0.2555 to 0.258 (time step = 511–515, $Fr = 0.28$), where the ship advanced 0.258 ship lengths and is thus still in a strong transient. The non-linear iterations are limited to 10 or stopped when the residual decreases to 10^{-5} in all variables. At a later stage, when close to the steady-state solution, the solution changes little between time steps and the number of non-linear iterations reduces to typically 3.

The air/water interface elevation compared with experimental data for $Fr = 0.28$ is shown in Figure 11. The numerical results compare very well with the experimental values near the hull. Farther out the Kelvin wave is diffused, as expected for this relatively coarse double-O grid. It must be stressed also that a significant number of the grid points are used to resolve the air flow and thus are not used on the computation of the water flow.

At a higher speed the wavelength of the Kelvin wave increases significantly, and then coarser grids can be used to match the wave pattern. However, a breaking overturning bow wave is present at $Fr = 0.41$, and very fine grids are needed to resolve this feature. In Figure 12 a comparison of the wave field obtained with GFM/HFM and a solution on a fine grid (3.84 million grid points)

DOI: 10.1002/fld

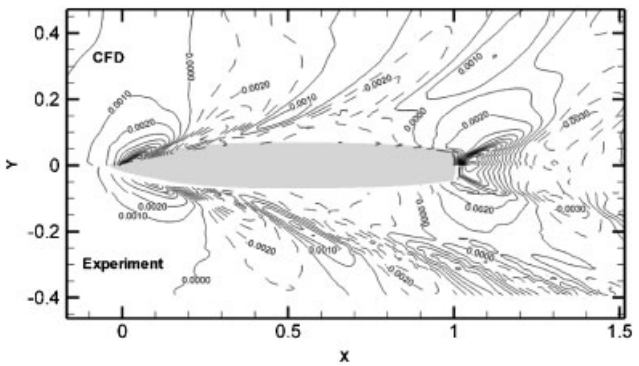

Figure 11. Wave elevation for $Fr = 0.28$.

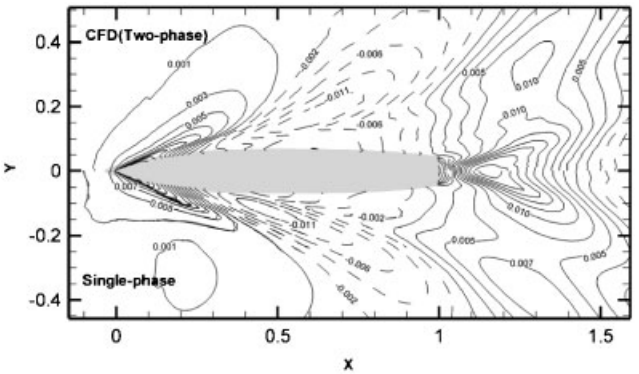

Figure 12. Wave elevation for $Fr = 0.41$.

using single-phase level set is shown. The single-phase level set solution was obtained using overset grids with special refinements on the bow region to capture the breaking wave, and on the interfacial region to better resolve the Kelvin pattern [31]. The main features of the Kelvin wave pattern including the bow wave and shoulder waves are displayed clearly and the general results are good. The coarser grid used for GFM/HFM is unable to capture the overturning bow wave, though the bow wave is very steep and shows signs of incipient breaking. The quality of the air/water interface solution is also good in the stern region.

Figure 13 shows the wave profiles at the hull surface. The solution for $Fr = 0.28$ compares well with experiments everywhere except at the bow, where the wave elevation is underpredicted by about 25%; the single-phase results using a fine grid with overset refinement are better in the bow region [58]. The underprediction of the bow wave is more marked for $Fr = 0.41$, with the rest of the profile adequately predicted. The wave profile obtained with a single-phase level set method and overset grid refinements to capture the breaking bow wave [31] is also shown for $Fr = 0.41$. At the bow and stern the single-phase solution compares better with experiments, while in the mid-section of the ship the GFM/HFM solution is better. It must be noted that the presence of the breaking wave does not seem to have a large effect on the resistance coefficient, but it significantly

DOI: 10.1002/fld

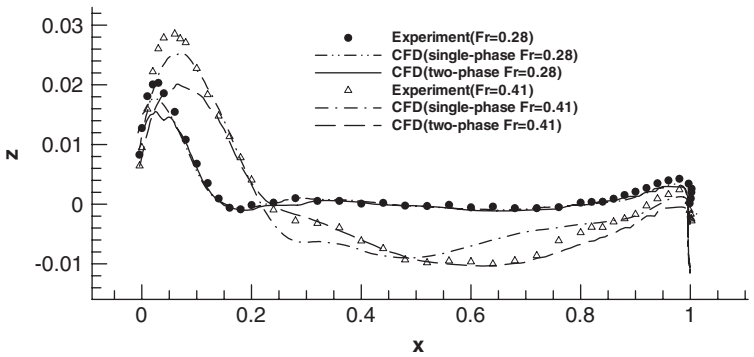

Figure 13. Wave profiles at the hull.

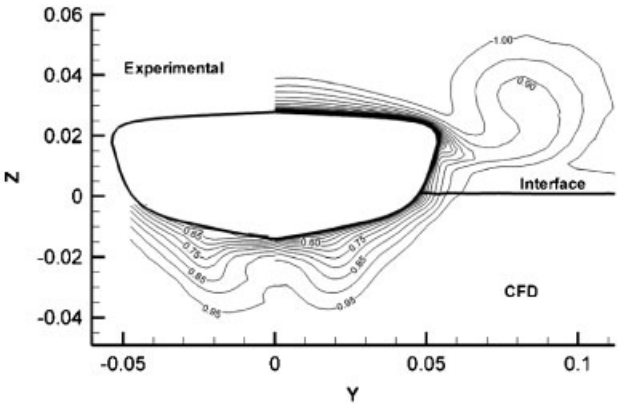

Figure 14. Axial velocity (u) contour at the nominal wake plane.

affects the wave field [31]. It is expected that finer grids, and mainly overset refinements, will greatly improve the quality of the prediction of the surface wave profiles, as with other methods; see for instance, the studies for this geometry with different codes at the Tokyo Workshop [55].

Experimental PIV measurements of the 3D velocity field at the propeller plane $x = 0.935$ (the nominal wake) have been reported by Gui *et al.* [56], Longo and Stern [57]. Figure 14 shows the axial velocity contours at the nominal wake plane for both CFD and experiments. The agreement between the experimental data and the GFM/HFM method is at the same level of quality as the single-phase solver, while also resolving the air flow. The model properly captures the bulging of the boundary layer caused by interaction between the sonar dome tip vortex and the boundary layer. The CFD solution also shows the velocity contours in air, which seems reasonable though no experimental data are available. A momentum defect is observed also in the air, caused by a vortex detached from the bow in the air and its interaction with the air boundary layer. This deck edge vortex has been observed on computations in frigates and carriers (see for instance [4]) and can cause instabilities detrimental to safe aircraft landings.

DOI: 10.1002/fld

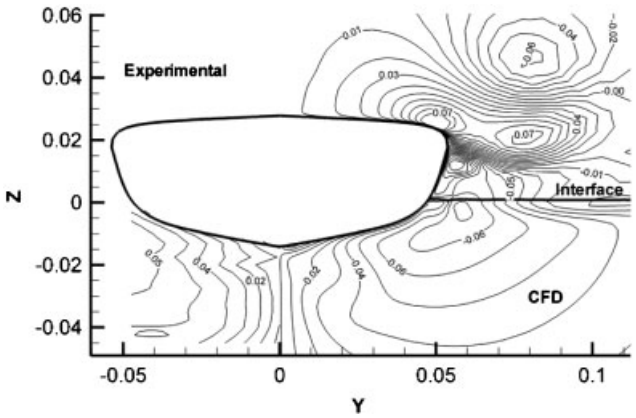

Figure 15. Transversal (v) velocity contour at the nominal wake plane.

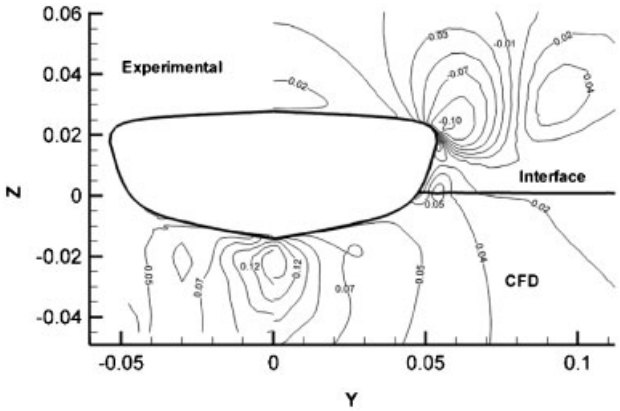

Figure 16. Vertical (w) velocity contour at the nominal wake plane.

The transverse and vertical velocities in the nominal wake plane are shown in Figures 15 and 16. Again, the agreement with the experimental data in water is excellent. Note the very good level of continuity of the velocity field across the air/water interface for all three components of the velocity. This indicates that the presence of spurious velocities is minimal, overcoming one of the main problems of many two-phase level set methods when treating high density ratios [22, p. 355], mainly in distorted curvilinear grids [32].

It is of interest to evaluate how well the turbulence model behaves when used simultaneously in air and water. Since the resistance is largely dominated by the water flow (about 1% is due to the air flow), and comparison with experimental data at the nominal wake plane was good, we conclude that the turbulence model performs at least acceptable in water. No data are available in air, and thus no validation is possible.

It must be noted here that, since the Reynolds number in air is about 15 times smaller than the Reynolds number in water, at model scale most boundary layers will have significant laminar

DOI: 10.1002/fld

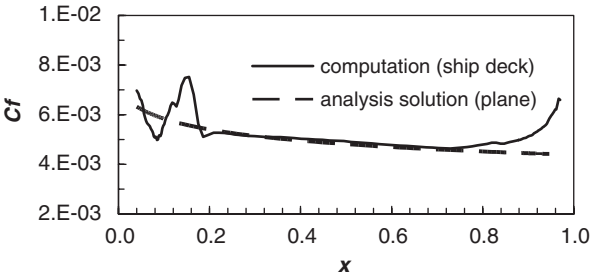

Figure 17. Axial distribution of friction coefficient in air at the centreplane on the deck ($Fr = 0.28$).

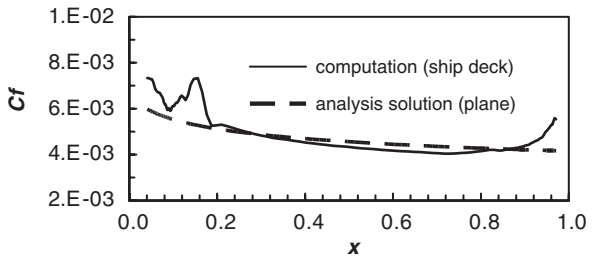

Figure 18. Axial distribution of friction coefficient in air at the centreplane on the deck ($Fr = 0.41$).

sections in air, unless the turbulence is tripped. In our computations we used a fully turbulent model. Accurate predictions in air would need the implementation of a low Reynolds number turbulence model. At full scale this is not an issue since the Reynolds numbers are much higher and the flow will be fully turbulent everywhere.

Although the ship deck is a little bit curvilinear in the bow and rear region, the most part is very close to a flat surface, therefore, it is useful to validate the turbulent boundary layer in air by comparing the computational results on the central line of ship deck with the approximate analytical solution of the local shear-stress coefficient for a flat plate.

In Figures 17 and 18 distributions of the local shear-stress coefficient on the centreline of the deck are shown for $Fr = 0.28$ and 0.41, respectively, from where we can see that the difference between computational results and analytical solution is small in the region $0.2 < x < 0.8$, where the deck is essentially flat and the inlet and exit geometry changes do not have much influence. The local shear-stress coefficient adopted is

$$c_f = \frac{\tau_x}{0.5(\rho_a/\rho_l)} \tag{81}$$

where

$$\tau_x = \frac{\mu}{Re}\left(\frac{\partial u_1}{\partial x_j} + \frac{\partial u_j}{\partial x_1}\right) n_j$$

DOI: 10.1002/fld

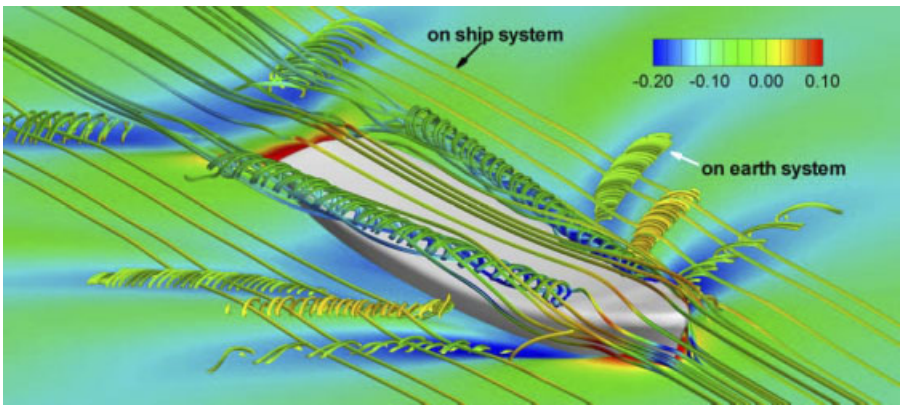

Figure 19. Streamlines and air/water interface ($Fr = 0.28$).

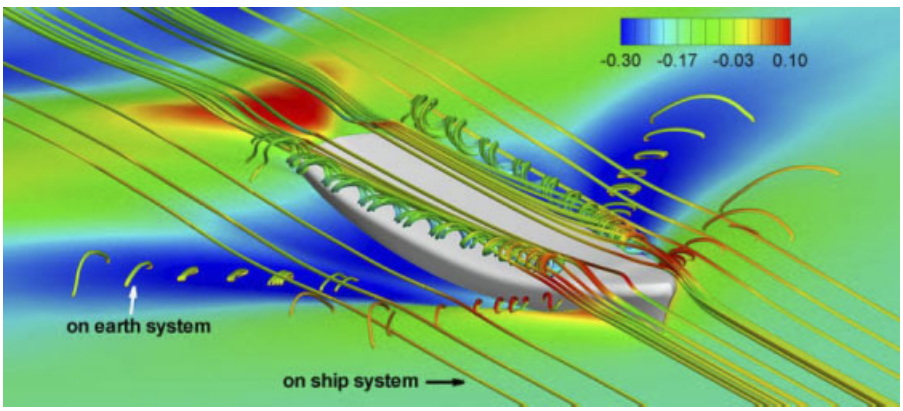

Figure 20. Streamlines and air/water interface ($Fr = 0.41$).

is the dimensionless shear stress. The analytical solution used is

$$c_f = 0.027(Re_x)_{\text{air}}^{-1/7} \tag{82}$$

Figures 19 and 20 show the air/water interface and streamlines in the air region for the cases with $Fr = 0.28$ and 0.41, respectively. Streamlines based on the ship coordinate system and on an earth fixed coordinate system are shown. The streamlines are coloured by axial velocity in the earth fixed coordinate system. The streamlines on the earth coordinate were obtained by generating Q isosurfaces and drawing streamlines attached to those isosurfaces. Note the ability of the GFM to capture the orbital velocity caused by the waves, and the deck edge vortices detaching from the bow region. These vortices cause a wake shown clearly in Figures 14–16. The streamlines based on the ship system are smooth in the far field region and just above the deck, but exhibit significant curvature near the bow and stern regions of the ship. The streamlines based on the earth system clearly show the local vortices in the air region around the ship, where a pair of axial vortices

DOI: 10.1002/fld

originally detach from the bow region of the deck. Vortices are also clearly shown on the interface at the crest and troughs, mainly on the bow, stern and shoulder waves.

5. CONCLUSIONS AND FURTHER WORK

A coupled ghost fluid/Heaviside function method (GFM/HFM) was developed for body-fitted structured grids to simulate air/water turbulent flows, with the focus on ship hydrodynamics. The model and numerical methods were validated for three cases: super- and sub-critical steady-state flow without wave breaking and an impulsive plunging wave breaking flow over 2D submerged bumps, and the 3D flow around a ship model DTMB 5512, including a deck. The results show good agreement with the experimental data and single-phase level set results in finer grids.

The proposed method features a sharp interface for the pressure gradient and density with zero transition thickness, and overcomes the difficulties shown by the standard level set method based on Heaviside functions for relatively large grid spacing. Piezometric pressure was adopted as an independent variable to solve Navier–Stokes and continuity equation, thus eliminating the gravity forces from the momentum equation and allowing an easier balance between pressure and gravity forces. Approximate jump conditions are derived for piezometric pressure and velocity, and pressure gradients in curvilinear grids based on the exact continuous velocity and stress and jump in momentum conditions with jump in density maintained but continuity of molecular and turbulent viscosities imposed. A projection method in a collocated grid was adopted to solve the Poisson equation resulting from enforcing mass conservation. To reinitialize the level set function, a fast marching method was developed for curvilinear grids.

Current and near future work is focused on two lines. First improvements to the GFM/HFM method will be studied, including higher-order jump conditions, exact jump conditions for turbulent flow, and Lagrangian methods for the level set function transport and reinitialization. The second line of work, and possibly the most important, is the implementation of static and dynamic overset grids capabilities for the coupled GFM/HFM method. This is specially important in ship hydrodynamics since this would enable dramatic improvements in the quality of the results, as already demonstrated in the single-phase level set methods, when the overset grids are used for local discretization to capture breaking waves and high Froude number Kelvin waves. In addition, dynamic overset will enable the ability of performing ship motions calculations.

ACKNOWLEDGEMENTS

This research was sponsored by Office of Naval Research grant N00014-01-1-0073 under the administration of Dr Patrick Purtell. Runs were performed on the IBM Power 4 machines at the DoD NAVO MSRC.

REFERENCES

1. Wilson RV, Carrica PM, Stern F. Unsteady RANS method for ship motions with application to roll for a surface combatant. *Computers and Fluids* 2006; **35**(5):501–524.
2. Carrica PM, Wilson RV, Stern F. An unsteady single-phase level set method for viscous free surface flows. *International Journal for Numerical Methods in Fluids* 2007; **53**:229–256.
3. Reddy KR, Toffoletto R, Jones KRW. Numerical simulation of ship airwakes. *Computers and Fluids* 2000; **29**:451–465.

DOI: 10.1002/fld

4. Nangia RK, Lumsden RB. Novel vortex flow devices-columnar vortex generators studies for airwakes. *Thirty-fourth AIAA Fluid Dynamics*, Portland, OR, U.S.A., 28 June–1 July 2004; 1–18.
5. Syms GF. Numerical simulation of frigate airwakes. *International Journal of Computational Fluid Dynamics* 2004; **18**:199–207.
6. Moat BI, Yelland MJ, Pascal RW, Molland AF. Quantifying the airflow distortion over merchant ships. Part I: Validation of a CFD model. *Journal of Atmospheric and Oceanic Technology* 2006; **23**:341–350.
7. Moat BI, Yelland MJ, Molland AF. Quantifying the airflow distortion over merchant ships. Part II: Application of the model results. *Journal of Atmospheric and Oceanic Technology* 2006; **23**:351–360.
8. Hirt CW, Nichols BD. Volume of fluid (VOF) method for dynamics of free boundaries. *Journal of Computational Physics* 1981; **39**:201–221.
9. Youngs DL. Time-dependent multimaterial flow with large fluid distortion. In *Numerical Methods for Fluid Dynamics*, Morton K, Baines M (eds). Academic Press: New York, 1982; 273–285.
10. Harvie DJE, Fletcher DF. A new volume of fluid advection algorithm: the stream scheme. *Journal of Computational Physics* 2000; **162**:1–32.
11. Kim MS, Lee WI. A new VOF-based numerical scheme for the simulation of fluid with free surface. Part I: New free surface-tracking algorithm and its verification. *International Journal for Numerical Methods in Fluids* 2003; **42**:765–790.
12. Lopez J, Hernandez J, Gomez P, Faura F. An improved PLIC-VOF method for tracking thin fluid structures in incompressible two-phase flows. *Journal of Computational Physics* 2005; **208**:51–71.
13. Azcueta R, Muzaferija S, Peric M. Computation of breaking bow wave for a very full hull ship. *Seventh International Conference on Numerical Ship Hydrodynamics*, Nantes, France, 1999.
14. Klemt M. RANSE simulation of ship seakeeping using overlapping grids. *Ship Technology Research* 2005; **52**:65–81.
15. Tryggvason G, Bunner B, Esmaeeli A, Juric D, Al-Rawahi N, Tauber W, Han J, Nas S, Jan YJ. A front-tracking method for the computation of multiphase flows. *Journal of Computational Physics* 2001; **169**:708–759.
16. Jacqmin D. Calculation of two-phase Navier–Stokes flows using phase-field modeling. *Journal of Computational Physics* 1999; **155**:96–127.
17. Rhee SH, Skinner C. Unstructured grid based Navier–Stokes solver for free surface flow around surface ships. In *Proceedings of CFD Workshop*, Hino T (ed.). National Maritime Research Institute of Japan: Tokyo, Japan, 2005; 504–509.
18. el Moctar O, Schellin TE, Priebe T. CFD and FE methods to predict wave loads and ship structural response. *Twenty-sixth Symposium on Naval Hydrodynamics*, Rome, Italy, 17–22 September 2006.
19. Osher S, Sethian JA. Fronts propagating with curvature-dependent speed: algorithms based on Hamilton–Jacobi formulations. *Journal of Computational Physics* 1988; **79**:12–49.
20. Sussman M, Smereka P, Osher S. A level set approach for computing solutions to incompressible two-phase flow. *Journal of Computational Physics* 1994; **114**:146–159.
21. Osher S, Fedkiw R. Level set method: an overview and some recent results. *Journal of Computational Physics* 2001; **169**:463–502.
22. Sethian JA, Smereka P. Level set method for fluid interface. *Annual Review of Fluid Mechanics* 2003; **35**:341–372.
23. Sussman M, Fatemi E. An efficient, interface-preserving level set redistancing algorithm and its application to interfacial incompressible fluid flow. *SIAM Journal on Scientific Computing* 1999; **20**:1165–1191.
24. Sethian JA. Fast marching methods. *SIAM Review* 1999; **41**:199–235.
25. Enright D, Fedkiw R, Ferziger J, Mitchell I. A hybrid particle level set method for improved interface capturing. *Journal of Computational Physics* 2002; **183**:83–116.
26. Sussman M. A second order coupled level set and volume-of-fluid method for computing growth and collapse of vapor bubbles. *Journal of Computational Physics* 2003; **187**:110–136.
27. Vogt M, Larsson L. Level set method for predicting viscous free surface flows. *Seventh International Conference on Numerical Ship Hydrodynamics*, Nantes, France, 1999.
28. Di Mascio A, Broglia R, Muscari R. On the application of the single-phase level set method to naval hydrodynamic flows. *Computers and Fluids* 2007; **36**:868–886.
29. Carrica PM, Wilson RV, Stern F. Unsteady RANS simulation of the ship forward speed diffraction problem. *Computers and Fluids* 2006; **35**:545–570.
30. Carrica PM, Wilson RV, Stern F. Ship motions using single-phase level set with dynamic overset grids. *Computers and Fluids* 2007, in press.
31. Wilson RV, Carrica PM, Stern F. Simulation of a ship breaking bow wave and induced vortices and scars. *International Journal for Numerical Methods in Fluids* 2007. DOI: 10.1002/fld.1406

32. Cura Hochbaum A, Vogt M. Towards the simulation of seakeeping and maneuvering based on the computation of the free surface viscous ship flow. *Twenty-fourth ONR Symposium on Naval Hydrodynamics*, Fukoka, Japan, 2002.
33. Fedkiw R, Aslam T, Xu S. The ghost fluid method for deflagration and detonation discontinuities. *Journal of Computational Physics* 1999;
34. Liu XD, Fedkiw R, Kang M. A boundary condition capturing method for Poisson's equation on irregular domains. *Journal of Computational Physics* 2000; **160**:151–178.
35. Kang M, Fedkiw R, Liu XD. A boundary condition capturing method for multiphase incompressible flow. *Journal of Scientific Computing* 2000; **15**:323–360.
36. Liu H, Krishnan S, Marella S, Udaykumar HS. Sharp interface cartesian grid method II: A technique for simulating droplet interactions with surfaces of arbitrary shape. *Journal of Computational Physics* 2005; **210**:32–54.
37. Pijl SP, Segal A, Vuik C, Wesseling P. A mass-conserving level-set method for modelling of multi-phase flows. *International Journal for Numerical Methods in Fluids* 2005; **47**:339–361.
38. Moureau VM, Minot P, Berat C, Pitsch H. A ghost-fluid method for large-eddy simulations of premixed combustion in complex geometries. *Annual Research Briefs*, Center for Turbulence Research, 2005; 269–282.
39. Shin S. Internal wave computations using the ghost fluid method on unstructured grid. *International Journal for Numerical Methods in Fluids* 2005; **47**:233–251.
40. Zhou YC, Zhao S, Feig M, Wei GW. High order matched interface and boundary method for elliptic equations with discontinuous coefficients and singular sources. *Journal of Computational Physics* 2006; **213**:1–30.
41. Wang WC. A jump condition capturing finite difference scheme for elliptic interface problems. *SIAM Journal on Scientific Computing* 2004; **25**:1479–1496.
42. Thompson JF, Warsi ZUA, Mastin JW. *Numerical Grid Generation*. North-Holland: Amsterdam, 1985.
43. Menter FR. Two-equation eddy viscosity turbulence models for engineering applications. *AIAA Journal* 1994; **32**:1598–1605.
44. Drew DA, Passman SL. *Theory of Multicomponent Fluids*. Applied Mathematical Sciences. Springer: New York, 1999; 135.
45. Bell JB, Colella P, Howell LH. An efficient second-order projection method for viscous incompressible flow. *Tenth AIAA Computational Fluid Dynamics Conference*, Honolulu, June 1991; 24–27.
46. Adalsteinsson D, Sethian JA. The fast construction of extension velocities in level set method. *Journal of Computational Physics* 1999; **148**:2–22.
47. Sethian JA. Numerical methods for propagating interfaces: Hamilton–Jacobi equations and conservation laws. *Journal of Differential Geometry* 1990; **31**:131–161.
48. Sethian JA. A fast marching level set method for monotonically advancing fronts. *Proceedings of the National Academy of Sciences*, 1996; **93**:1591–1595.
49. Cahouet J. Etude numerique er experimentale du probleme bidimensionnel de la resistance de vaques non-lineaire. *Ph.D. Thesis*, ENSTA, Paris, 1984 (in French).
50. Vogt M. A comparison between moving grid and a level set technique for solving 2D free surface flows. *The 1997 ASME Fluids Engineering Division Summer Meeting FEDSM'97*, 22–26 June 1997.
51. Iafrati A, Di Mascio A, Campana EF. A level set technique applied to unsteady free surface flows. *International Journal for Numerical Methods in Fluids* 2001; **35**:281–297.
52. Xing T, Kandasamy M, Wilson RV, Stern F. DES and RANS of unsteady free-surface flows. *Proceedings of the 42nd AIAA Aerospace Sciences Meeting*, Division for Fluid Dynamics, Reno, NV, 2004.
53. Stern F, Huang J, Carrica PM, Yang J, Ghosh S, Van S. Two-phase level set CFD and PIV EFD for plunging breaking waves, including alternative CFD approaches and extensions for air/water ship flow. *Twenty-sixth Symposium on Naval Hydrodynamics*, Rome, Italy, 17–22 September 2006.
54. Larsson L, Stern F, Bertram V. Benchmarking of computational fluid dynamics for ship flows: the Gothenburg 2000 Workshop. *Journal of Ship Research* 2003; **47**:63–81.
55. Hino T (ed.). In *Proceedings of CFD Workshop*. National Maritime Research Institute: Tokyo, Japan, 2005.
56. Gui L, Longo J, Stern F. Towing tank PIV measurement system, data and uncertainty assessment for DTMB model 5512. *Experiments in Fluids* 2001; **31**:336–346.
57. Longo J, Stern F. Uncertainty assessment for towing tank tests with example for surface combatant DTMB model 5512. *Journal of Ship Research* 2005; **49**:55–68.
58. Miller R, Gorski J, Wilson RV, Carrica PM. RANS simulation of a naval combatant using a single-phase level set method with overset grids. In *Proceedings of CFD Workshop*, Hino T (ed.). National Maritime Research Institute of Japan: Tokyo, Japan, 2005; 575–580.

DOI: 10.1002/fld